INTERNATIONAL JOURNAL FOR NUMERICAL METHODS IN FLUIDS, VOL. 3, 71–92 (1983)

# NUMERICAL SOLUTION OF VISCOUS FLOWS USING INTEGRAL EQUATION METHODS

M. B. BUSH AND R. I. TANNER

*Department of Mechanical Engineering, The University of Sydney, N.S.W., Australia 2006*

## SUMMARY

A formulation of the boundary element method for the solution of non-zero Reynolds number incompressible flows in which the non-linear terms are lumped together to form a forcing function is presented. Solutions can be obtained at low to moderate Reynolds numbers. The method was tested using the flow of a fluid in a two-dimensional converging channel (Hamel flow) for which an exact solution is available. An axisymmetric formulation is demonstrated by examining the drag experienced by a sphere held stationary in uniform flow. Performance of the method was satisfactory. New results for an axisymmetric free jet at zero Reynolds number obtained using the boundary element method are also included. The method is ideal for this type of free-surface problem.

KEY WORDS Boundary Elements Hamel Flow Free Surface

## 1. INTRODUCTION

Direct implementation of boundary integral equation methods has received a great deal of attention over the last decade in the expectation that these methods would have the ability to handle certain classes of problems without the large storage requirements and computational effort associated with classical finite element methods. Initial development and implementation of these methods in two- and three-dimensional elastostatics appears to be due to Rizzo[1] and Cruse.[2] The basis of the method is flexible and has allowed boundary integral formulations to be applied to a wide variety of linear and non-linear problem classes[3] including elastodynamics,[4] analysis of composite materials,[5] anisotropic materials,[6] elasto-plastic deformation problems[7] and low Reynolds number fluid dynamics.[8–10]

The present report describes a 'pseudo-body force' implementation (treating the non-linear terms as forcing functions) of the integral equation method in plane and axisymmetric co-ordinates. This represents a new application of this well-known technique to the problem of solving non-zero Reynolds number flows of a Newtonian, incompressible fluid. The treatment is analogous to the successful elasto-plasticity work of Banerjee and Cathie;[7] further examples and references are given in Brebbia.[3] The method provides a solution that is effectively a regular perturbation of Reynolds number for arbitrary geometry. This work represents ongoing research by the authors[10] and forms a basis for more sophisticated treatments of this problem and other non-linear fluid mechanics problems such as non-Newtonian fluid mechanics.

In the first section of the paper we derive the relevant integral equations from the governing equations of motion. Subsequent sections give details of the numerical treatment and solution scheme used. Finally, we demonstrate the new method by presenting the numerical examples of flow between converging planes (Hamel's problem) and evaluation of

0271–2091/83/010071–22$02.20

*Received 29 January 1981*
*Revised 12 April 1982*

the drag on a sphere in an infinite medium; the potential of the method for solving free surface problems is also demonstrated by an example.

## 2. GOVERNING EQUATIONS OF MOTION

To define the terminology used throughout this report the governing equations are summarized in this section. The equations of motion and mass conservation for an incompressible, Newtonian viscous fluid can be written using Cartesian tensor notation as follows:

$$\frac{\partial \sigma_{jk}}{\partial x_k}+\rho(f_j-a_j)=0 \tag{1}$$

$$\frac{\partial u_k}{\partial x_k}=0 \tag{2}$$

where $\sigma_{jk}$ is the stress tensor, $u_k$ are the velocity components, $\rho$ is the fluid density, $f_j$ are arbitrary body forces per unit mass and $a_j$ are the acceleration components per unit mass. Under steady state conditions the $a_j$ are given by

$$a_j=u_k\frac{\partial u_j}{\partial x_k} \tag{3}$$

The stress tensor can be written as

$$\sigma_{jk}=-p\delta_{jk}+2\mu d_{jk} \tag{4}$$

where $p$ is the pressure,, $\delta_{jk}$ is the Kronecker delta function which is unity if $j=k$ and zero if $j\neq k$, $\mu$ is the (constant) viscosity and $d_{jk}$ is the rate of strain tensor given by

$$d_{jk}=\frac{1}{2}\left(\frac{\partial u_j}{\partial x_k}+\frac{\partial u_k}{\partial x_j}\right) \tag{5}$$

Both $\sigma_{jk}$ and $d_{jk}$ are symmetric tensors.

To these equations are added boundary conditions; either the traction (force per unit area) or the velocity will be specified over the fluid boundaries.

## 3. INTEGRAL REPRESENTATION OF THE GOVERNING EQUATIONS

In this section we use a weighted residual statement as the starting point for development of the required integral equations, and the treatment follows closely the treatment given to the equivalent elasticity problem by Brebbia.[11]

Consider a set of arbitrary velocity, pressure and stress weighting fields signified by $u_j^*$, $p^*$ and $\sigma_{ij}^*$. If conditions (1) and (2) are not satisfied identically in some region $\Omega$ and the boundary conditions only approximately satisfied on the boundary $\Gamma$ of the region then the following weighted residual statement can be written:

$$\int_\Omega\left\{\frac{\partial \sigma_{jk}}{\partial x_k}+\rho(f_j-a_j)\right\}u_j^*\,\mathrm{d}\Omega+\int_\Omega\frac{\partial u_k}{\partial x_k}\mathrm{p}^*\,\mathrm{d}\Omega+\int_{\Gamma_1}(u_j-\hat{u}_j)t_j^*\,\mathrm{d}\Gamma-\int_{\Gamma_2}(t_j-\hat{t}_j)u_j^*\,\mathrm{d}\Gamma=0 \tag{6}$$

where $t_j$ is a traction vector $\sigma_{jk}n_k$ formed from $\sigma_{jk}$ and the unit outward normal vector components $n_k$ at the surface, $\hat{u}_j$ are the velocity components given as boundary conditions on the sections of $\Gamma$ represented by $\Gamma_1$ and $\hat{t}_j$ are the traction components given as boundary conditions on $\Gamma_2$ (where $\Gamma_1+\Gamma_2=\Gamma$, the whole surface). Since (6) will vanish for any solution satisfying (1) and (2) and the boundary conditions, (6) must be true for arbitrary (*) fields when the unstarred field is the true solution to the problem in hand.

If the solution satisfies the boundary conditions fully then the governing equations are only approximately satisfied in $\Omega$, giving rise to conventional finite element formulations. However, if the boundary conditions are approximately satisfied and the weighting functions chosen such that they satisfy the equations of motion and continuity, boundary integral formulations are obtained.[11]

In the present work the (*) fields are taken to be Newtonian and incompressible. After integrating (6) by parts the integral equation becomes

$$\int_\Omega \frac{\partial u_k}{\partial x_k} p^* \, d\Omega - \int_\Omega \sigma_{jk} \frac{\partial u_j^*}{\partial x_k} \, d\Omega = \rho \int_\Omega (a_j - f_j) u_j^* \, d\Omega$$

$$- \int_{\Gamma_1} (u_j - \hat{u}_j) t_j^* \, d\Gamma - \int_{\Gamma_1} t_j u_j^* \, d\Gamma - \int_{\Gamma_2} \hat{t}_j u_j^* \, d\Gamma \tag{7}$$

Equation (7) can be reduced in the following manner. Since $\sigma_{jk}$ and $d_{jk}$ (hence $\sigma_{jk}^*$ and $d_{jk}^*$) are symmetric, the second term in (7) can be written in the following form:

$$\int_\Omega \sigma_{jk} \frac{\partial u_j^*}{\partial x_k} \, d\Omega = \int_\Omega \sigma_{jk} d_{jk}^* \, d\Omega. \tag{8}$$

The integrand in (8) can be expanded using (4) to give

$$\int_\Omega \sigma_{jk} d_{jk}^* \, d\Omega = -\int_\Omega p \frac{\partial u_k^*}{\partial x_k} \, d\Omega + 2\mu \int_\Omega d_{jk} d_{jk}^* \, d\Omega \tag{9}$$

If the true and (*) fields in (9) are interchanged then the following results:

$$\int_\Omega \sigma_{jk}^* d_{jk} \, d\Omega = -\int_\Omega \frac{\partial u_k}{\partial x_k} p^* \, d\Omega + 2\mu^* \int_\Omega d_{jk}^* d_{jk} \, d\Omega \tag{10}$$

where $\mu^*$ is the viscosity of the Newtonian (*) field. Since the (*) field is chosen to be incompressible then the first term on the right-hand side of (9) vanishes and if $\mu^* = \mu$ (9) and (10) can be combined to yield

$$\int_\Omega \sigma_{jk} d_{jk}^* \, d\Omega - \int_\Omega \frac{\partial u_k}{\partial x_k} p^* \, d\Omega = \int_\Omega \sigma_{jk}^* d_{jk} \, d\Omega \tag{11}$$

This is a reciprocal theorem for incompressible viscous flow.[8,9] Integration by parts can again be used to yield:

$$\int_\Omega \sigma_{jk}^* d_{jk} \, d\Omega = \int_\Gamma t_j^* u_j \, d\Gamma - \int_\Omega \frac{\partial \sigma_{jk}^*}{\partial x_k} u_j \, d\Omega \tag{12}$$

and substituting into (7) gives

$$\int_\Omega \frac{\partial \sigma_{jk}^*}{\partial x_k} u_j \, d\Omega = \rho \int_\Omega (a_j - f_j) u_j^* \, d\Omega + \int_\Gamma u_j t_j^* \, d\Gamma - \int_\Gamma t_j u_j^* \, d\Gamma \tag{13}$$

In (13) it is understood that $u_j = \hat{u}_j$ on $\Gamma_1$ and $t_j = \hat{t}_j$ on $\Gamma_2$. The left-hand side of (13) can be further reduced by choosing the (*) fields such that

$$\frac{\partial \sigma_{jk}^*}{\partial x_k} + \Delta(P)\delta_{ij} = 0 \tag{14}$$

where $\Delta(P)$ is the Dirac delta function at the point $P$ in the domain $\Omega$ and $\delta_{ij}$ is the Kronecker delta function. The (*) field therefore satisfies Stokes' equations in an infinite domain with a unit point source of momentum in the $i$ direction at $P$ and the solution of (14) is the familiar 'Stokeslet'.[12,13]

It is useful to elaborate the terminology at this stage for purposes of clarity. If the Stokeslet force oriented in the $i$ direction is at $P$ then we represent by $u_{ij}^*(P, Q)$ the $j$ component of the corresponding velocity at $Q$. Similarly, the traction field at a boundary point $Q$ is written as $t_{ij}^*(P, Q)$. Using this terminology and substituting (14) into (13) gives

$$u_i(P) = \rho\int_\Omega \{f_j(Q) - a_j(Q)\}u_{ij}^*(P, Q)\,\mathrm{d}\Omega + \int_\Gamma t_j(Q)u_{ij}^*(P, Q)\,\mathrm{d}\Gamma - \int_\Gamma u_j(Q)t_{ij}^*(P, Q)\,\mathrm{d}\Gamma \quad (15)$$

The result (15) is general for two- and three-dimensional cases; it can also be used to represent problems in axisymmetric co-ordinates if (14) is solved for the case of a unit source of momentum distributed evenly around a ring. Solutions for the equivalent elasticity problem are presented incompletely by Kermanidis[14] and Cruse *et al.*[15] The complete solution in the form used for the present investigation is shown in Appendix I.

Equation (15) provides an expression for the velocity field at any interior point $P$ and can provide a suitable expression for $P$ lying on the boundary $\Gamma$ by allowing $P$ to become a boundary point. However, the equation contains integrals that are singular when $P$ coincides with $Q$. The integrals involving $u_{ij}^*(P, Q)$ are weakly singular and do not require special treatment whereas the integral involving $t_{ij}^*(P, Q)$ is strongly singular when $P$ lies on the boundary and exists only as a principal value.[16] The jump corresponding to the strongly singular integral has been dealt with in the literature[2,3,5,15] and equation (15) can be written in the general form:

$$C_{ij}u_j(P) = \rho\int_\Omega \{f_j(Q) - a_j(Q)\}u_{ij}^*(P, Q)\,\mathrm{d}\Omega + \int_\Gamma t_j(Q)u_{ij}^*(P, Q)\,\mathrm{d}\Gamma - \int_\Gamma u_j(Q)t_{ij}^*(P, Q)\,\mathrm{d}\Gamma \quad (16)$$

where $C_{ij} = \delta_{ij}$ if $P$ lies in the domain $\Omega$ and if $P$ is a point on the boundary $\Gamma$ the value of $C_{ij}$ depends on the smoothness of the boundary. For a smooth boundary at $P$, $C_{ij} = \frac{1}{2}\delta_{ij}$. (By smooth we mean that at the point $P$ the boundary has a continuous profile with no sharp corners.)

Equation (16) provides the required relationship between the velocity field at any point $P$, the surface values of velocity and traction and a body force term. The appearance of the non-linear acceleration terms $a_j$ in the body force integral suggests the name 'pseudo-body force' as an apt description of the formulation. Since $a_j$ depends on the velocity field, the pseudo-body force is not known prior to solution and an iterative scheme must be used. The solution scheme used in the present work is described in a later section.

An equation similar to (16) (with more complicated kernels) can be written for internal stresses (see Brebbia[11]) and hence, by summing the direct stresses, the internal pressures can be found. This equation can be used to evaluate internal stresses once the body forces are known; however, this is not pursued in this report.

The velocity gradients required for evaluation of $a_j$ can be obtained directly by differentiating (16). However, since the velocity field must also be computed and the gradients are required at a large number of interior points, we have chosen to use a finite element approximation to evaluate the gradients. This is described in the following section.

## 4. DISCRETIZATION OF THE INTEGRAL EQUATIONS

Numerical implementation of (16) requires discretization of the boundary into a number of 'boundary elements' and discretization of the interior into a number of 'internal cells' as shown in Figure 1. The boundary elements used are geometrically linear and the functions (velocity and traction) are assumed to be constant on each element. As shown in Figure 2 only one centrally located node needs to be associated with an element where ${}_nu_j$ and ${}_nt_j$ are the velocity and traction components at the $n$th node ($n$th element).

The internal velocity field is approximated by evaluating the velocity components at each interior node (Figure 1). The velocity field at any interior point can then be approximated by interpolating between the vertices of each internal cell. The velocity gradients are approximated by assigning to each cell a value of gradient obtained by differentiating the linear interpolating function. A value can then be assigned to each cell vertex by averaging the values contributed by all cells sharing this vertex. This averaging procedure was found to be necessary since it distributes the errors more evenly and provides a much improved approximation of the gradient at the vertex. The velocity gradients at any interior location are then obtained by interpolating between the vertices of the relevant cell. An alternative approach to computing the gradients is to differentiate (16) and evaluate the new boundary and domain integrals. However, the former approach obviously involves far less computational effort and was found to provide adequate results.

Following discretization of the boundary Γ into $N$ elements of the type shown in Figure 2

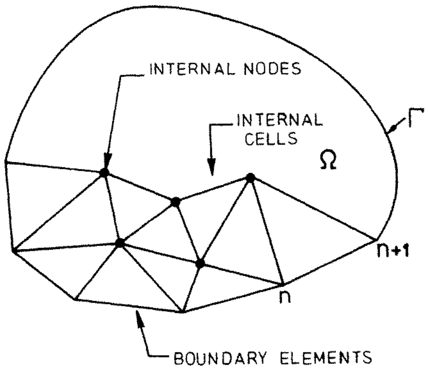

Figure 1. Discretization of boundary Γ and domain Ω into elements and cells. A typical boundary element bounded by points $n$ and $n+1$ is shown in Figure 2

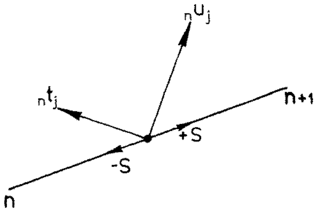

Figure 2. The 'constant' boundary element corresponding to the $n$th node. The node is located centrally on the element and has tractions ${}_nt_j$ and velocities ${}_nu_j$

and the region $\Omega$ into $M$ cells as shown in Figure 1, equation (16) can be written as

$$C_{ij}u_j(P)+\sum_{n=1}^{N}{}_nu_j\int_{\Gamma_n}t_{ij}^*(P,Q)\,\mathrm{d}\Gamma=\rho\sum_{m=1}^{M}\int_{\Omega_m}b_j(Q)u_{ij}^*(P,Q)\,\mathrm{d}\Omega+\sum_{n=1}^{N}{}_nt_j\int_{\Gamma_n}u_{ij}^*(P,Q)\,\mathrm{d}\Gamma \quad (17)$$

where $b_j(Q)=f_j(Q)-a_j(Q)$ is the total body force, $\Omega_m$ refers to the $m$th internal cell, $\Gamma_n$ refers to the $n$th boundary element and $P$ refers to a node. This can be rewritten in matrix/vector form as

$$H\mathbf{u}=G\mathbf{t}+\mathbf{b} \quad (18)$$

where $\mathbf{u}$ and $\mathbf{t}$ are vector assemblages of ${}_nu_j$ and ${}_nt_j$ on the boundary, $\mathbf{b}$ is a vector corresponding to the body force terms and $H$ and $G$ are coefficient matrices composed of integrals of $t_{ij}^*(P,Q)$ and $u_{ij}^*(P,Q)$ respectively over individual boundary elements.

In a well-posed problem the number of unknown components of $\mathbf{u}$ and $\mathbf{t}$ combined should equal the number of prescribed values and (18) can be accordingly rearranged to give:

$$A\mathbf{x}=\mathbf{y}+\mathbf{b} \quad (19)$$

In (19), $\mathbf{x}$ represents the unknown boundary values, $A$ is the resulting matrix of coefficients and $\mathbf{y}$ is a known vector incorporating the prescribed boundary values. For a plane or axisymmetric well-posed problem $\mathbf{x}$, $\mathbf{y}$ and $\mathbf{b}$ are all $2N\times 1$ vectors and $A$ is of order $2N\times 2N$. The matrix $A$ is fully populated and generally not symmetrical or diagonally dominant. It is therefore not amenable for specialized direct or iterative solution procedures and for a given $\mathbf{b}$ (19) is best solved using Gaussian elimination.

Once the boundary solution has been obtained, (17) can be used to provide the velocity field at any interior node. If there are $L$ such nodes then the interior velocity field solution can be written in matrix/vector form as

$$\mathbf{v}=R\mathbf{t}-S\mathbf{u}+\mathbf{c} \quad (20)$$

where $\mathbf{v}$ is a $2L\times 1$ vector representing the internal solutions, $\mathbf{t}$ and $\mathbf{u}$ are the $2N\times 1$ boundary vectors as given in (18), $R$ and $S$ are coefficient matrices of order $2L\times 2N$ and $\mathbf{c}$ is a $2L\times 1$ vector representing the non-linear terms.

An iterative scheme can now be devised using (19) and (20). However, before proceeding with this we give some details of evaluation of the integrals appearing in (17).

## 5. COMPUTATION OF THE INTEGRALS

In this section we discuss the numerical treatment given to the integrals in equation (17). Two cases need to be considered: (a) the point $P$ does not lie on the boundary element or internal cell in question and (b) $P$ lies on the element or cell. In case (a) the singularity in the kernels $u_{ij}^*(P,Q)$ and $t_{ij}^*(P,Q)$ does not lie in the interval or region of integration and ordinary Gaussian quadrature can be applied. In case (b), however, the singular characteristics of the kernels require the special treatment described below.

### *5.1. Integration along boundary segments*

When the point $P$ corresponds to the $n$th boundary node and integration is being performed along the $n$th element as shown in Figure 2, the kernels in both plane and axisymmetric co-ordinates contain singularities of order $\ln|s|$ and $1/s$. Owing to the simple form of the kernels in plane co-ordinates, the integration can be performed analytically.[7,11] However, the axisymmetric kernels are significantly more complicated and are treated by extracting the leading singular terms and integrating these in exact form. The remainder of the kernel is then integrated using standard Gaussian quadrature.

### 5.2. *Integration over internal cells*

Two possible situations arise. The first is the case where the source point $P$ coincides with the vertex of a cell and occurs during computation of the internal velocity field. The second case is where $P$ lies on the edge of a cell and occurs during preparation of the boundary solution. However, the second case can be considered as a repetitive application of the first case and does not require separate treatment.

When the source point $P$ coincides with a vertex of the $m$th cell, the integral over that cell can be written as:

$$\int_{\Omega_m} b_j(Q)u_{ij}^*(P,Q)\,\mathrm{d}\Omega = \int_{\Omega_m} \{b_j(Q)-b_j(P)\}u_{ij}^*(P,Q)\,\mathrm{d}\Omega + b_j(P)\int_{\Omega_m} u_{ij}^*(P,Q)\,\mathrm{d}\Omega \tag{21}$$

In (21) $\{b_j(Q)-b_j(P)\}$ uniformly approaches zero as $Q$ approaches $P$ and at least partially counters the weakly singular behaviour of $u_{ij}^*(P,Q)$. The first integral on the right-hand side of (21) is then more amenable to numerical integration. For the plane problem the second integral on the right-hand side of (21) can be performed in exact form and analytical expressions are presented in Appendix II. The axisymmetric problem is not handled as easily and it is necessary to extract only the leading singular term from $u_{ij}^*(P,Q)$ ($\ln(w)$, where $w$ is the separation of $P$ and $Q$) and rewrite (21) as

$$\int_{\Omega_m} b_j(Q)u_{ij}^*(P,Q)\,\mathrm{d}\Omega = \int_{\Omega_m} \{b_j(Q)u_{ij}^*(P,Q)-C_i(P)\ln(w)\}\,\mathrm{d}\Omega + C_i(P)\int_{\Omega_m} \ln(w)\,\mathrm{d}\Omega \tag{22}$$

where $b_j(Q)u_{ij}^*(P,Q)-C_i(P)\ln(w)$ is bounded as $Q$ approaches $P$. The second integral on the right-hand side of (22) is given in Appendix II.

## 6. SOLUTION SCHEME

The solution scheme used in the present investigation based on equations (19) and (20) is as follows. If the superscript $n$ indicates the $n$th approximation of the solution then the updated boundary solution is given by

$$A\mathbf{x}^{n+1} = \mathbf{y} + \mathbf{b}^n \tag{23}$$

and the updated velocity field solution is then obtained using

$$\mathbf{v}^{n+1} = R\mathbf{t}^{n+1} - S\mathbf{u}^{n+1} + \mathbf{c}^n \tag{24}$$

The starting solution is obtained by setting **b** and **c** to zero, thereby providing the zero Reynolds number solution for the particular geometry and boundary conditions.

Such a scheme of lumping the non-linear inertia terms together to act as forcing function in (23) is expected to fail to converge once inertia becomes the dominant effect and in similar finite element schemes this occurs at very low values of Reynolds number.[17] A solution obtained in this manner can therefore be regarded as a regular perturbation of Reynolds number for arbitrary geometry. However, we note that $A$ does not change during iteration and need be eliminated only once, provided a record of the elimination procedure is retained. Furthermore, the order of $A$ depends on the number of boundary elements and not on the number of internal cells. Most of the computational effort is involved with evaluation of **b** and **c** and this is readily controlled by variation of the grid coarseness. We therefore propose that the method presently described is a useful means of obtaining non-zero Reynolds number solutions and we proceed to demonstrate its use.

## 7. EXAMPLES OF SOLVED PROBLEMS

In this section we present the solutions to some problems obtained using the boundary integral equation method described. The first problem treated is that of an axisymmetric, Newtonian free jet at zero Reynolds number (zero density fluid). These results provide a test of the kernels presented in Appendix I for axisymmetric problems (see also Bush and Tanner[10]) and demonstrate successful extension of the program to handle free surface flows.

The second problem treated is the Hamel flow problem with non-zero Reynolds number. This is a mildly non-linear problem that has an exact solution for comparison with the numerical results. Finally, the drag on a sphere held in a uniform flow is examined at low Reynolds number.

All numerical solutions were obtained using CDC Cyber 170–730 computer operating in single precision.

### *7.1. Axisymmetric jet*

Boundary element solutions of the expansion of a plane, Newtonian free jet have previously been presented.[8,9] The boundary discretization used for the equivalent axisymmetric problem is shown in Figure 3 where $Z$ is the distance measured from the exit plane, $R$ is the radius of the jet at any $Z$ and $R_0$ is the nozzle radius. The numerical boundary conditions applied correspond to fully developed Poiseuille flow upstream, no-slip velocity conditions on the nozzle and zero normal and tangential traction conditions on the free surface and downstream boundary. Figure 3 shows the starting geometry, which corresponds to a plug flow.

The method of finding the free surface geometry was to first solve the problem with the prescribed boundary conditions and starting geometry. The assumed free surface will generally not describe a stream surface and the computed normal velocity will not be zero. The free surface geometry is correspondingly updated and the process repeated until convergence has occurred. Convergence was rapid with little change occurring after 4 updates; the final jet expansion was 12·84 per cent. Figure 4 shows the final jet geometry (after 4 iterations) compared with a least-squares curve fitted to experimental data by

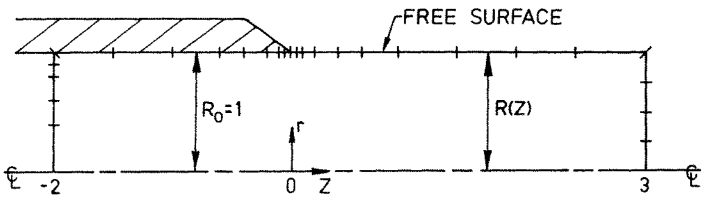

Figure 3. Discretization of the jet boundary. The number of boundary elements is 27 (—+— indicates the end points of elements)

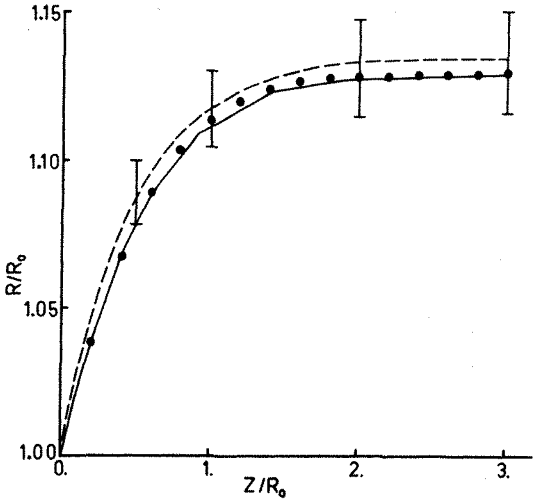

Figure 4. Comparison of computed jet shape (——) with other numerical results from AXFINR[19] (●) and the experiments of Batchelor and Horsfall[18](– – –). The bars indicate approximate spread of measurements

Batchelor and Horsfall[18] and numerical results obtained using the AXFINR finite element program (see Nickell, *et al.*[19]). Agreement with the experimental results is satisfactory and agreement between the numerical results is excellent.

One of the most difficult features of this problem to capture numerically is the stress singularity at the exit lip of the jet. If a finite element program is to be used to model this problem a fine mesh in the region of the lip is required to follow the rapid variations in stress. The total number of degrees of freedom in the problem is correspondingly large. The boundary element method however allows a fine boundary discretization to be used near the lip without a large increase in the number of unknown quantities to be evaluated. The stress can then be evaluated at any chosen interior location. In Figure 5 the dimensionless tensile stress $\sigma_{zz}R_0/\mu\bar{u}$, where $\bar{u}$ is the average axial velocity, is plotted against radius $r$ at the jet exit plane and the difficulty in modelling such a problem is readily apparent. It is interesting

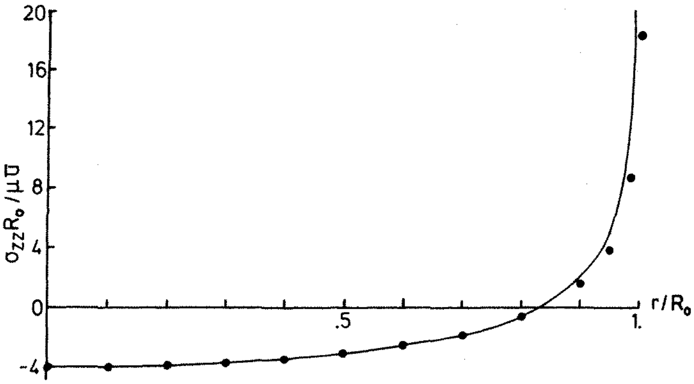

Figure 5. Dimensionless tensile stress $\sigma_{zz}R_0/\mu\bar{u}$ across jet exit plane computed using AXFINR[19] (●) and boundary elements (——)

to note that the AXFINR program was run using 2928 degrees of freedom whereas the boundary element program used only 54. The latter required only 2 per cent of the execution time of AXFINR to obtain the jet shape.

### *7.2. Hamel flow problem*

The flow of a fluid between two infinite flat plates set at an angle as shown in Figure 6 is termed the Hamel problem, after one of the first investigators of the problem, and a comprehensive discussion of Hamel flow is given by Batchelor.[20] This problem provides a means of testing numerical solution schemes since it is a steady state flow in which the inertia terms do not vanish identically (as they do in flow between infinite parallel plates and Poiseuille flow) and an exact solution can be obtained for comparison with numerical results. For these reasons the Hamel problem was used as a test example by Gartling *et al.*[17] in a finite element convergence study, and we have chosen to use it as a comparative test of the present solution method.

7.2.1. *Theory.* For study of the Hamel problem it is useful to use polar co-ordinates $(r, \theta)$ where $r$ is the distance from the intersection of the two walls and $\theta$ is measured from the centreline (Figure 6). The exact solution of the problem is based on the assumption of purely radial flow which yields self-similar velocity profiles at all radii. The product of centreline velocity $u_0$ and radius $r$ is constant. This allows the Reynolds number for the flow to be defined as

$$\mathrm{Re} = \frac{\alpha u_0 r \rho}{\mu} \tag{25}$$

which is constant throughout the flow field for a given half angle $\alpha$, density $\rho$ and viscosity $\mu$.

The analysis of Batchelor[20] leads to the following identity governing Hamel flow:

$$1 = \int_0^1 \frac{\mathrm{d}f}{(1-f)^{1/2}\{\frac{2}{3}\alpha\,\mathrm{Re}\,(f^2+f-2)+4\alpha^2 f+c\}^{1/2}} \tag{26}$$

where $f$ is the ratio of radial velocity $u_r(r, \theta)$ to centreline velocity $u_0$ and $c$ is constant. A numerical representation of the exact solution obtained from (26) using an iterative, numerical quadrature process is reported by Gartling *et al.*[17] and was used to provide the 'exact' solutions given in the present report. For given values of $\alpha$, $\rho$, $\mu$ and flow rate/unit length (flux) the procedure provides updated approximations of the Reynolds number until the computed flux matches the prescribed flux. The velocity profiles can then be computed.

The case of zero Reynolds number flow (zero density fluid) can be solved analytically. The

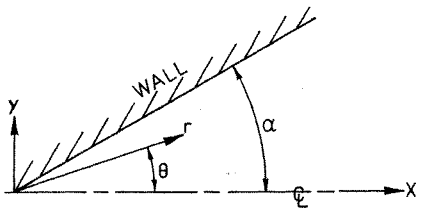

Figure 6. Hamel flow problem—sink or source located at the origin of co-ordinates

problem reduces to one of solving the following differential equation:

$$\frac{d^3f}{d\eta^3}+4\alpha^2\frac{df}{d\eta}=0 \tag{27}$$

where $\eta=\theta/\alpha$. The solution of (27) is

$$u_r(r,\theta)=u_0\frac{\cos(2\alpha\eta)-\cos(2\alpha)}{1-\cos(2\alpha)}. \tag{28}$$

The centreline velocity $u_0$ can be evaluated for a given flux using

$$\text{Flux}=\alpha r\int_{-1}^{1}u_r(r,\eta)\,d\eta. \tag{29}$$

7.2.2. *Numerical results.* For the results presented in this section $\alpha=30°$, $\mu=1$, flux$\,=1$ (in the half wedge $\theta=0$ to $\theta=\alpha$) and the Reynolds number was varied by changing $\rho$. Purely convergent flow (inflow) is considered.

Since only a finite length of wedge geometry can be modelled by the numerical procedure, a set of boundary conditions had to be applied to the upstream and downstream ends of the wedge. This presented a difficulty since the conditions here are not known exactly and must be approximated. Velocity boundary conditions corresponding to zero Reynolds number flow were applied on the upstream end of the wedge to provide the required flux through the wedge-shaped region. At the medium values of Reynolds number considered in this work the influence of this boundary condition approximation affects the solution in the immediate neighbourhood of the boundary but the disturbance dies away some distance downstream. We show later that ample undisturbed regions exist downstream, providing approximations of the exact solution. Zero traction boundary conditions were applied on the downstream end of the wedge which again introduce a small disturbance. This disturbance dies away a small distance upstream. No-slip velocity conditions were prescribed on the plate wall and symmetry conditions on the centreline. The section of the wedge considered in the numerical calculations was the region between the radius $r=\frac{1}{4}$ and $r=4$.

The three different grid patterns used are shown in Figure 7(a), Figure 7(b) and Figure 7(c). In all cases the number of boundary elements remained fixed at $N=32$; the particular boundary discretization is shown in Figure 7(a) where the side of a cell lying on the boundary represents a boundary element. The three different meshes Grid 1, Grid 2 and Grid 3 therefore represent a variation in approximation of the internal velocity field, having $M=96$, $M=54$ and $M=28$ internal cells respectively.

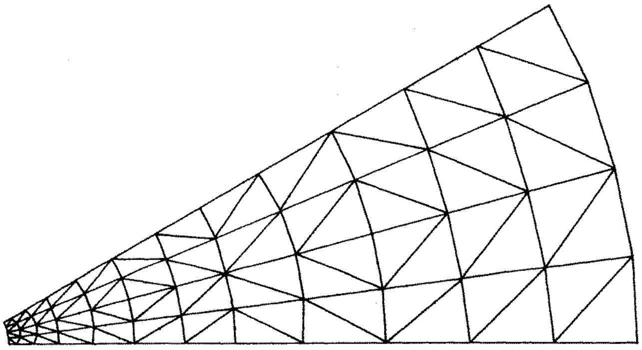

Figure 7(a). Grid 1—32 boundary elements, 96 cells

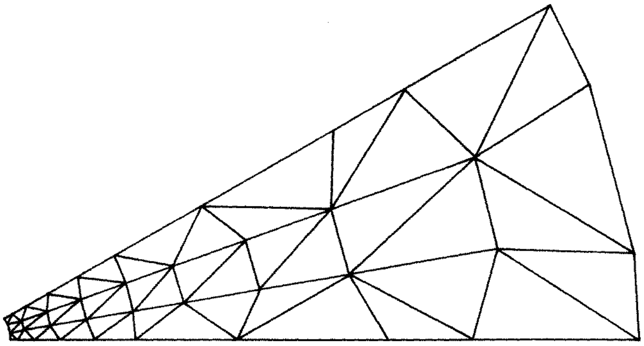

Figure 7(b). Grid 2—32 boundary elements, 54 cells

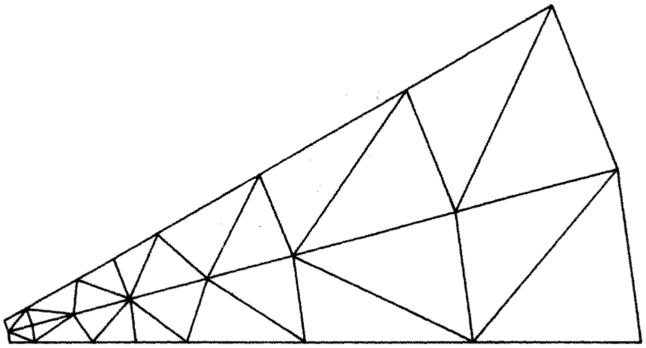

Figure 7(c). Grid 3—32 boundary elements, 28 cells

In order to provide a measure of the computational effort needed to produce the non-linear solution relative to the linear solution of the particular problem, a comparison can be made between the computation time required for each iteration in the non-linear solution and the time required to obtain the creeping solution. The ratio of the former to the latter on Grid 1, Grid 2 and Grid 3 was 1·6, 1·0 and 0·5 respectively. It should be remembered that the creeping solution (the first iteration in the non-linear solution) involves complete assembly and elimination of the coefficient matrix whereas subsequent iterations require only back substitution after the pseudo-body forces have been integrated. In view of this one would expect that most of the computational effort per iteration in the non-linear solution is involved with evaluation of the body force integrals. The amount of time required for the creeping solution relative to subsequent iterations will therefore increase as the number of boundary elements is increased relative to the number of internal cells.

The following series of results correspond to the Reynolds number $\mathrm{Re} = 10{\cdot}9$ for which convergent solutions were obtained with all grids. Iteration was terminated on satisfaction of the inequality

$$\underset{1 \leq i \leq k}{\mathrm{MAX}} |v_i^{n+1} - v_i^n| \leq 5 \times 10^{-3} \tag{30}$$

where $k$ is the number of internal velocity degrees of freedom. Of primary interest is the

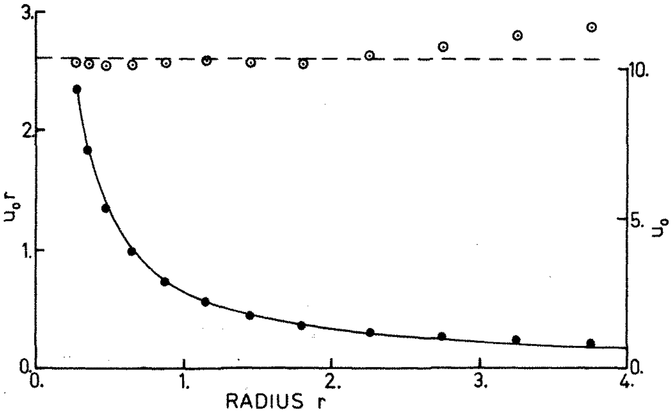

Figure 8. Radial variation of centreline speed $u_0$ and the product $u_0r$ on Grid 1, Re = 10·9. ---, true value of $u_0r$; ——, true $u_0$ profile; ⊙, nodal values of $u_0r$; ●, nodal values of $u_0$

influence on the numerical solution of the upstream and downstream boundary condition approximations. To observe this we have plotted in Figure 8 the radial variation of centreline speed $u_0$ and of the product $u_0r$ for Grid 1. It is clear that the downstream approximation has little obvious effect on the solution. However, as seen in the plot of $u_0r$, the upstream approximation is influencing the solution in the vicinity of this boundary but dies away sufficiently within 3 elements to leave an effectively constant value of $u_0r$ as expected. The corresponding functions plotted from Grid 2 and Grid 3 showed a similar behaviour and are not presented.

Figure 9 shows the variation of $|u_x|$ (the absolute value of $u_x$) at a radius $r = 1$ as a function of normalized angle $\theta/\alpha$. Since the present formulation uses linear interpolation of velocity between nodal values, a piecewise linear approximation of the true shape of the solution is

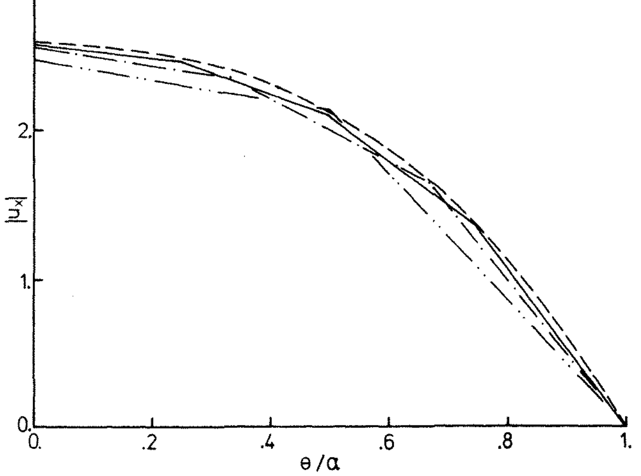

Figure 9. Profile of $|u_x|$ at $r = 1$, Re = 10·9. ---, exact solution; ——, Grid 1; ——·——, Grid 2; ——··——, Grid 3

obtained. It can be seen that as more internal nodes are used the nodal solutions are on the whole closer to the exact solution. This fact, together with the better piecewise linear approximation of the curve obtained, gives an overall better numerical representation of the exact solution and demonstrates the convergence of the solution method. The largest nodal error of 4·6 per cent occurs on Grid 3 at the centreline. Figure 10 shows the variation of $|u_y|$ at the radius $r = 1$ for Grid 1, and indicates that the discretization scheme is not sufficient to provide an adequate approximation of the maximum absolute value of $u_y$. If a better approximation was required, Figure 10 could be used to decide how the grid should be modified.

In order to accelerate iterative convergence where necessary an overrelaxation facility was built into the code that operates on successive internal velocity field solutions. Figure 11 shows the centreline speed $u_0$ at $r = 1$ as a function of iteration number for Grid 1. Iteration zero is the creeping (zero Reynolds number) solution. Relaxation factors of $\frac{1}{4}$, $\frac{1}{2}$ and 1 were tested. The figure indicates that convergence of the numerical solution at this point is most rapid with a relaxation factor of $\frac{1}{2}$. However, this is not true for all points in the mesh since the number of iterations required to satisfy (30) with relaxation factors of $\frac{1}{4}$, $\frac{1}{2}$ and 1 were 15, 8 and 6 respectively. Figure 11 indicates that use of a relaxation factor less than $\frac{1}{2}$ with Grid 1 at this Reynolds number causes over-damping and slow convergence.

The behaviour of the velocity profile ($u_x$) on Grid 1 at the radius $r = 1$ without relaxation is shown in Figure 12 where simple oscillating behaviour can be seen. The number of iterations required for (30) to be satisfied without relaxation on Grid 1, Grid 2 and Grid 3 were 6, 5 and 4 respectively, as a consequence of the variation in degrees of freedom between the mesh patterns.

To observe the effect of higher Reynolds number on the numerical solution we considered only Grid 1 since it provides the best approximation. The solution was evaluated at various values of the Reynolds number between Re = 0 and Re = 30. The solution at a particular Reynolds number was obtained using the previous solution as the starting point for iteration. The results are plotted in Figure 13 where the centreline speed $u_0$ at $r = 1$ is shown as a function of Reynolds number. The behaviour seen in Figure 13 is not unpredictable since an

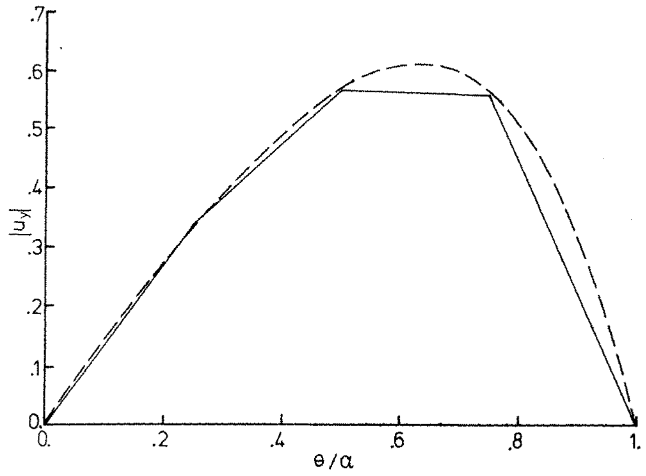

Figure 10. Profile of $|u_y|$ (——) on Grid 1 at $r = 1$, re = 10·9 compared with the exact solution (– – –)

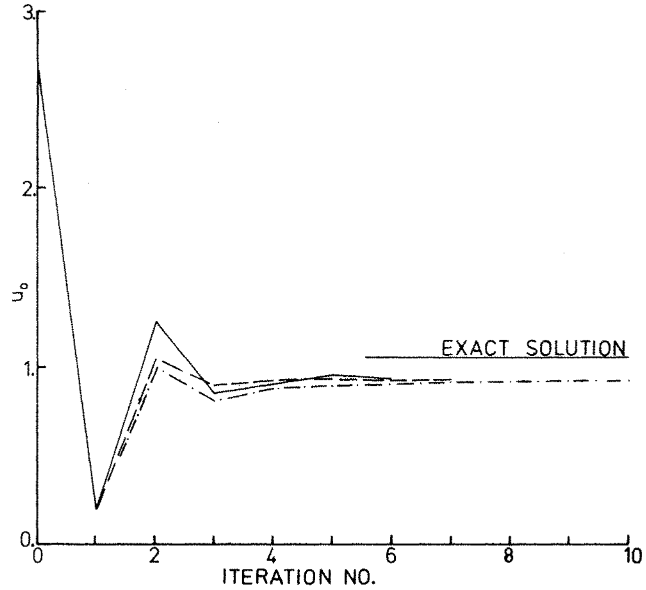

Figure 11. Behaviour of centreline speed $u_0$ on Grid 1 at $r = 1$, Re = 10·9 with various values of the overrelaxation factor $c$. ——, $c = 1$; – – –, $c = 0{\cdot}5$; —— · ——, $c = 0{\cdot}25$

increasingly less accurate solution at higher values of the Reynolds number is expected. At values of the Reynolds number greater than Re = 13 the numerical solution is significantly less than the exact solution, indicating departure from purely radial flow. This can be seen effectively in Figure 14, which shows the velocity profile ($|u_x|$) at $r = 1$ for Re = 29·8. Examination of the velocity vectors at the nodes indicated that the flow has departed significantly from purely radial flow to produce a numerical solution that lies below the exact

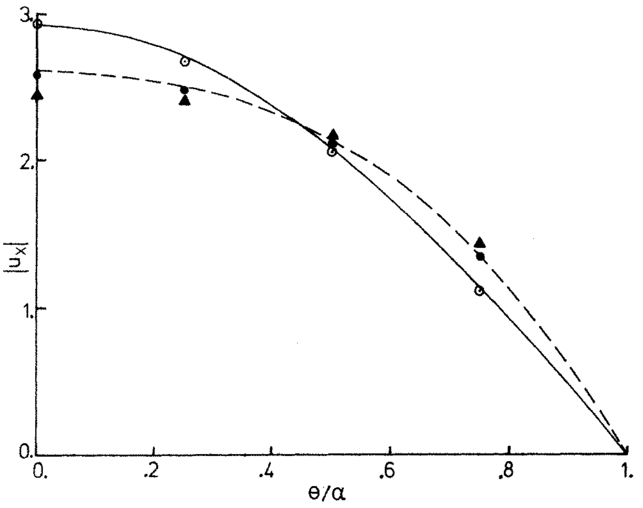

Figure 12. Behaviour of the velocity profile $|u_x|$ at $r = 1$, Re = 10·9 on Grid 1. No relaxation. ——, exact creeping solution; – – – exact solution for Re = 10·9; ⊙, iteration zero; ▲, iteration 1; ●, iteration 6

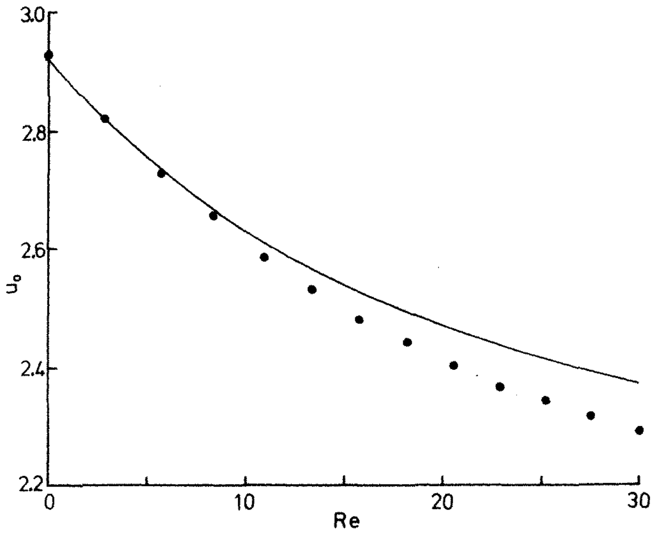

Figure 13. Comparison of the computed centreline speed $u_0$ at $r = 1$ on Grid 1 (●) with the exact values (——) for increasing Reynolds number Re

solution. The solution at the centreline is in error by 3·5 per cent and the grid is no longer sufficient to provide an adequate representation of the velocity field. It was found that the solution on this grid failed to converge above the Reynolds number Re = 34.

### 7.3. *Drag on a sphere held in uniform flow*

In this section we consider the more difficult problem of computing the drag experienced by a sphere held in uniform flow. Since boundary traction is one of the unknowns evaluated

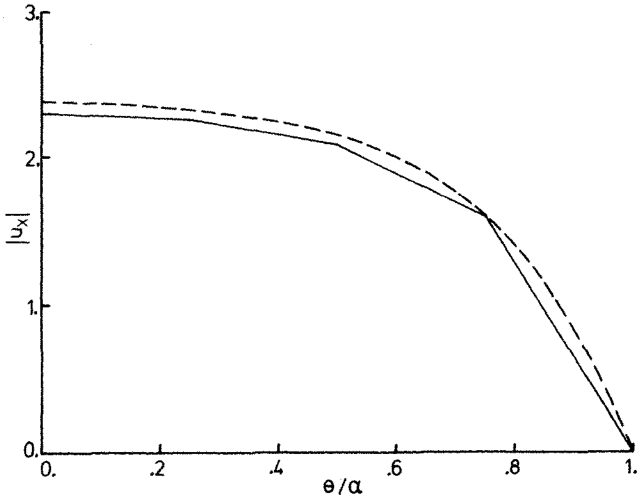

Figure 14. Comparison of the velocity profile $|u_x|$ on Grid 1 at $r = 1$, Re = 29·8 (——) with the exact solution (– – –)

directly by the boundary element method, the drag experienced by a surface can be found directly without the need for auxiliary computations.

Accurate measurements of sphere drag at low Reynolds numbers have been made by Maxworthy[21] where comparison between these and other experimental and theoretical results is made. The most interesting feature of this paper is the conclusion that the perturbation formula of Goldstein (see Van Dyke[22]) based on the Oseen linearization of the Navier–Stokes equations provides a better representation of the sphere drag trend for $\mathrm{Re} < 0{\cdot}9$ (based on sphere diameter) than the corresponding expansion for the full Navier–Stokes equations by Proudman and Pearson.[23] However, the latter provides a good approximation of the drag to the higher value $\mathrm{Re} = 1{\cdot}3$. For values of Reynolds number $\mathrm{Re} > 3$, Maxworthy[21] shows that the results presented by Perry[24] are adequate. In the present report the numerical results are compared with values given by Maxworthy for $\mathrm{Re} < 3$ and Perry[24] for $\mathrm{Re} > 3$.

The mesh pattern used is shown in Figure 15 where 100 cells provided the velocity field approximation. The two semicircular sections comprised the discretized boundaries containing 20 boundary elements. The axis of revolution does not require discretization to provide a solution since it represents a surface of zero area. The numerical boundary conditions applied were no-slip velocity conditions on the sphere and uniform flow conditions on the outer boundary. A uniform flow of $U = 1$ was applied parallel to the axis of revolution and zero traction conditions normal to the axis. The ratio of outer boundary radius to the sphere radius $a$ is 12.

Following the discussion of section 7.2.2 concerning computation time, one would expect that with the large number of internal cells relative to boundary elements in this problem, the computation time required for each iteration in the non-linear solution relative to the creeping solution will be correspondingly large. The value of this ratio was found to be 3·1.

It may be argued that such an arrangement of boundaries is actually modelling the flow caused by a sphere held stationary within a second moving sphere. However, this is not the case since the velocity normal to the axis of revolution on the outer boundary is not prescribed. To verify this we compared the computed zero Reynolds number drag experienced by the sphere with the theoretical Stokes drag of $6\pi\mu Ua$.[20] The relative difference between the computed value and the theoretical value for an infinite field was 5 per cent whereas the difference between the solution for the moving outer sphere case and the Stokes drag was 21 per cent. A further test was performed by extending the grid such that the ratio

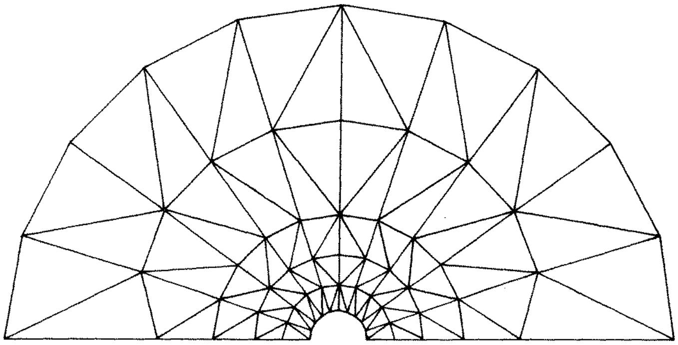

Figure 15. Boundary and field discretization for the sphere drag problem; 20 boundary elements, 100 cells

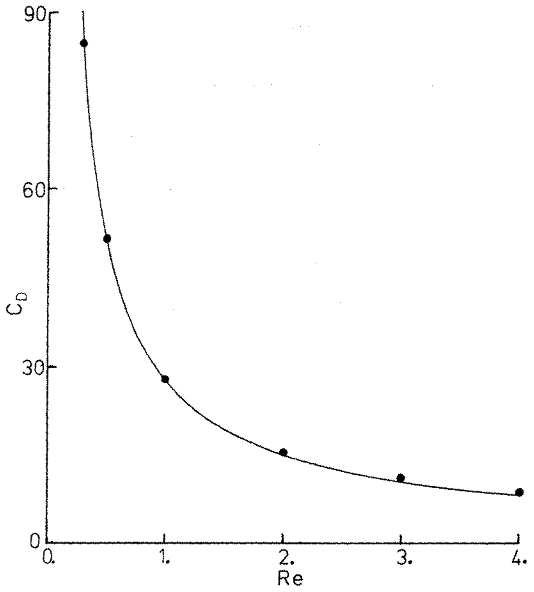

Figure 16. Comparison of computed drag coefficient (●) $C_D = \mathrm{DRAG}/(\pi a^2 \frac{1}{2}\rho U^2)$ with experimental results (——) of Maxworthy[21] (Re < 3) and Perry[24] (Re > 3) for various values of the Reynolds number $\mathrm{Re} = 2aU\rho/\mu$

of outer boundary radius to sphere radius was 24, twice the previous value. The computed Stokes drag was in error by 1·6 per cent, and the difference between the drag computed on each grid at the Reynolds number Re = 1 was less than 1 per cent. We are therefore confident that the boundary geometry shown in Figure 15 and boundary conditions used provide a reasonable approximation of the required flow at low Reynolds number. The solution at a given Reynolds number was obtained using the previous solution as the starting point. As shown in Figure 16 agreement is good up to the Reynolds number Re = 4. The results are also tabulated in Table I. Convergent solutions at higher values could not be obtained. However, solutions at the low values of Reynolds number for which the grid was intended are excellent and agree with the measurements of Maxworthy to within 5 per cent.

Table I. Sphere drag data (see Figure 16) together with relative error

| Re | $C_D$ Experimental | $C_D$ Numerical | Error % |
|---|---|---|---|
| 0·3 | 84·4 | 84·8 | 0·5 |
| 0·5 | 52·3 | 51·9 | 0·8 |
| 1·0 | 27·8 | 27·7 | 0·4 |
| 2·0 | 14·9 | 15·3 | 2·7 |
| 3·0 | 10·5 | 11·0 | 4·8 |
| 4·0 | 8·1 | 8·8 | 8·6 |

## 8. CONCLUSIONS; USE OF VELOCITY-TRACTION SCHEMES

In this paper we have described a formulation of the boundary element method that allows incompressible flow at non-zero Reynolds numbers to be handled. The purpose of the paper was to present some preliminary (but not exhaustive) test examples to indicate the success of the new method. The Hamel flow problem was used as the main test example since an exact solution exists. Performance of the program was satisfactory. The sphere drag problem provided a test of the axisymmetric part of the code once overall behaviour of the solution method was established on the Hamel problem. Performance was again satisfactory. The example of the axisymmetric free jet at zero Reynolds number provides the base for future examination of this problem at non-zero Reynolds number using the new method.

The discretization and functional approximation used in this work was the simplest possible. The present results indicate that the method is successful and that progression to the use of higher order elements would be warranted.

The failure to converge at higher Reynolds numbers is not unexpected. To avoid this problem one can envisage a VELOCITY-TRACTION method whereby internal velocities are evaluated as unknowns, together with the surface velocities and tractions already used. Then a successive substitution scheme can be used to find the solution, which will greatly enhance the chances of success at higher Reynolds numbers. Because of the accuracy in finding drag-coefficients due to the use tractions as direct solution variables, this scheme is considered a useful extension of the work presented here. A successive substitution solver has been implemented and is presently being tested.

ACKNOWLEDGEMENTS

We wish to thank Dr. J. F. Milthorpe for providing the finite element (AXFINR) solutions of the free jet problem for comparison.

## APPENDIX I. SINGULAR SOLUTIONS

### (i) *Plane problem*

The well-known Stokeslet in two dimensions is reproduced here for completeness.

$$u^*_{ij}(P, Q)=\frac{1}{4\pi\mu}\left\{-\ln(w)\delta_{ij}+\frac{\partial w}{\partial x_i}\frac{\partial w}{\partial x_j}\right\} \tag{31}$$

$$t^*_{ij}(P, Q)=-\frac{1}{\pi w}\left\{\frac{\partial w}{\partial n}\frac{\partial w}{\partial x_i}\frac{\partial w}{\partial x_j}\right\} \tag{32}$$

where $w$ is the distance between $P$ and $Q$ and $n$ is the unit outward normal vector.

### (ii) *Axisymmetric problem*

In the equations that follow, $z$ is the axial co-ordinate, $r$ is the radial co-ordinate, $(Z, R)$ are the co-ordinates of the ring source, $\mu$ is the viscosity, $Q_{-1/2}(k)$ and $Q_{1/2}(k)$ are Legendre's function of the second kind of degree $-\frac{1}{2}$ and $\frac{1}{2}$ respectively, and $k$ is given by

$$k=\frac{R^2+r^2+(Z-z)^2}{2Rr}. \tag{33}$$

The velocity kernels are given by:

$$
\begin{aligned}
C_6 u^*_{ZZ}(P, Q) &= \frac{1}{\mu\sqrt{(Rr)}}\left\{Q_{-1/2}(k) - \frac{(Z-z)^2}{Rr}\frac{\partial Q_{-1/2}}{\partial k}\right\} \\
C_6 u^*_{Zr}(P, Q) &= \frac{-(Z-z)}{2\mu r\sqrt{(Rr)}}\left\{Q_{-1/2}(k) + \frac{C_4}{Rr}\frac{\partial Q_{-1/2}}{\partial k}\right\} \\
C_6 u^*_{rZ}(P, Q) &= \frac{(Z-z)}{2\mu r\sqrt{(Rr)}}\left\{Q_{1/2}(k) - \frac{C_4}{Rr}\frac{\partial Q_{1/2}}{\partial k}\right\} \\
C_6 u^*_{rr}(P, Q) &= \frac{1}{\mu\sqrt{(Rr)}}\left\{Q_{1/2}(k) + \frac{(Z-z)^2}{Rr}\frac{\partial Q_{1/2}}{\partial k}\right\}
\end{aligned}
\tag{34}
$$

The traction kernels can be obtained using the surface normal vector $n_k$ and the tensor $\sigma^*_{ijk}(P, Q)$ (where $\sigma^*_{ijk}(P, Q)$ is the stress tensor component $\sigma_{jk}$ at $Q$ due to a unit source in direction $i$ at $P$) by forming

$$
t^*_{ij}(P, Q) = \sigma^*_{ijk}(P, Q) n_k \tag{35}
$$

where

$$
\begin{aligned}
C_6\sigma^*_{ZZZ}(P, Q) &= \frac{-2(Z-z)}{\sqrt{(Rr)}}\left\{\frac{(Z-z)^2}{C_1C_3}Q_{-1/2}(k) + \frac{4(Z-z)^2C_2}{RrC_1C_3}\frac{\partial Q_{-1/2}}{\partial k}\right\} \\
C_6\sigma^*_{ZZr}(P, Q) &= \frac{1}{r\sqrt{Rr)}}\left\{\frac{3C_4(Z-z)^2}{C_1C_3}Q_{1/2}(k) + \frac{(Z-z)^2}{Rr}\left[1 - \frac{4C_2C_4}{C_1C_3}\right]\frac{\partial Q_{1/2}}{\partial k}\right\} \\
C_6\sigma^*_{ZrZ}(P, Q) &= \frac{-1}{r\sqrt{(Rr)}}\left\{\frac{C_4(Z-z)^2}{C_1C_3}Q_{-1/2}(k) + \frac{(Z-z)^2}{Rr}\left[\frac{4C_2C_4}{C_1C_3} - 3\right]\frac{\partial Q_{-1/2}}{\partial k}\right\} \\
C_6\sigma^*_{Zrr}(P, Q) &= \frac{-(Z-z)}{r^2\sqrt{(Rr)}}\left\{\frac{3}{4}\left[1 - \frac{1}{C_1C_3}\langle C_4^2 - 4r^2(Z-z)^2\rangle\right]Q_{1/2}(k)\right. \\
&\qquad \left. + \frac{1}{Rr}\left[\frac{C_2}{C_1C_3}\langle C_4^2 - 4r^2(Z-z)^2\rangle - C_4\right]\frac{\partial Q_{1/2}}{\partial k}\right\} \\
C_6\sigma^*_{rrZ}(P, Q) &= \frac{-2(Z-z)}{r\sqrt{(Rr)}}\left\{\frac{1}{4r}\left[\frac{C_4^2}{C_1C_3} - 3\right]Q_{-1/2}(k) + \frac{C_4}{Rr^2}\left[\frac{C_2C_4}{C_1C_3} - \frac{3}{2}\right]\frac{\partial Q_{-1/2}}{\partial k}\right\} \\
C_6\sigma^*_{rrr}(P, Q) &= \frac{-1}{r\sqrt{(Rr)}}\left\{\frac{3C_4(Z-z)^2}{C_1C_3}Q_{1/2}(k) + \frac{1}{Rr}\left[2C_4 + (Z-z)^2\left\langle 3 - \frac{4C_2C_4}{C_1C_3}\right\rangle\right]\frac{\partial Q_{1/2}}{\partial k}\right\}.
\end{aligned}
\tag{36}
$$

where

$$
\begin{aligned}
C_1 &= (R+r)^2 + (Z-z)^2 \\
C_2 &= R^2 + r^2 + (Z-z)^2 \\
C_3 &= (R-r)^2 + (Z-z)^2 \\
C_4 &= R^2 - r^2 + (Z-z)^2 \\
C_5 &= R^2 - r^2 - (Z-z)^2 \\
C_6 &= 8\pi^2
\end{aligned}
\tag{37}
$$

## APPENDIX II. EXACT INTEGRATION OVER INTERNAL CELLS

The nomenclature for the following equations is shown in Figure 17 where the source point $P$ lies on a vertex of the $m$th internal cell signified by $\Omega_m$. Following (31) the integrals of $u^*_{ij}(P, Q)$ over $\Omega_m$ can be written in the form

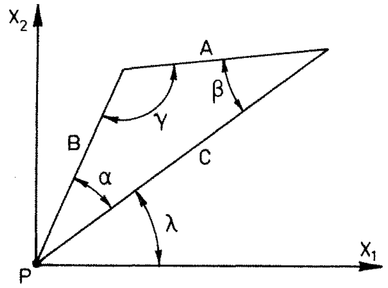

Figure 17. Nomenclature for exact integration

$$\int_{\Omega_m} u^*_{ij}(P, Q)\,\mathrm{d}\Omega = \frac{1}{4\pi\mu}\{I\delta_{ij} + J_{ij}\} \tag{38}$$

where $\delta_{ij}$ is the Kronecker delta function and

$$I = \int_{\Omega_m} -\ln(w)\,\mathrm{d}\Omega, \tag{39}$$

$$J_{ij} = \int_{\Omega_m} \frac{\partial w}{\partial x_j}\frac{\partial w}{\partial x_i}\,\mathrm{d}\Omega. \tag{40}$$

After converting to local polar co-ordinates with origin centred at $P$, integration yields:

$$I = -\tfrac{1}{2}C\sin(\beta)\{C\ln(C)\cos(\beta) + C\alpha\sin(\beta) - \tfrac{3}{2}\mathrm{A} + B\ln(B)\cos(\gamma)\} \tag{41}$$

$$J_{11} = \tfrac{1}{2}C^2\sin^2(\beta)\left\{\frac{A\cos^2(\lambda-\beta)}{B\sin(\gamma)} - \alpha\cos(2\lambda-2\beta) - \ln(C/B)\sin(2\lambda-2\beta)\right\} \tag{42}$$

$$J_{12} = \tfrac{1}{2}C^2\sin^2(\beta)\left\{\ln(C/B)\cos(2\lambda-2\beta) - \sin(2\lambda-2\beta)\left[\alpha - \frac{A}{2B\sin(\gamma)}\right]\right\} \tag{43}$$

$$J_{22} = \tfrac{1}{2}C^2\sin^2(\beta)\left\{\frac{A\sin^2(\lambda-\beta)}{\beta\sin(\gamma)} + \alpha\cos(2\lambda-2\beta) + \ln(C/B)\sin(2\lambda-2\beta)\right\}. \tag{44}$$

## REFERENCES

1. F. J. Rizzo, 'An integral equation approach to boundary value problems in classical elastostatics', *Q. Appl. Math.*, **25,** 83–95 (1967).
2. T. A. Cruse, 'Numerical solutions in three dimensional elastostatics', *Int. J. Solids Struct.*, **5,** 1295–1274 (1969).
3. C. A. Brebbia (ed.), *Boundary Element Methods*, Springer-Verlag, Germany, 1981.
4. T. A. Cruse and F. J. Rizzo, 'A direct formulation and numerical solution of the general transient elastodynamic problem' *Int. J. Math. Anal. Applic.*, **22,** 244 (1968).
5. T. A. Cruse and J. L. Swedlow, 'Interactive program for analysis and design problems in advanced composites technology', *AFML-TR-71-268* (1971).
6. F. J. Rizzo and D. J. Shippy, 'A method for stress determination in plane anisotropic elastic bodies', *J. Composite Materials.*, **4,** 36–61 (1970).

7. P. K. Banerjee and D. N. Cathie, 'A direct formulation and numerical implementation of the boundary element method for two-dimensional problems of elasto-plasticity', *Int. J. Mech. Sci.*, **22,** 233–245 (1980).
8. J. F. Milthorpe and R. I. Tanner, 'Boundary element methods for free surface viscous flows', *Proc. 7th Aust. Hyd. and Fluid Mech. Conf.*, Brisbane, Australia, 103–106 (1980).
9. R. I. Tanner, 'Application of boundary element methods to extrusion problems', *Proc. 2nd World Congress of Chemical Engineering, Montrèal, Canada*, 281–285 (1981).
10. M. B. Bush and R. I. Tanner, 'The boundary element method applied to the creeping motion of a sphere', *Proc. 2nd. Int. Conf. on Num. Meth. in Laminar and Turbulent Flow*, Venice, Italy, 119–128 (1981).
11. C. A. Brebbia, *The Boundary Element Method for Engineers*, Pentech Press, Great Britain, 1980.
12. Hidenori Hasimoto and Osamu Sano, 'Stokeslets and eddies in creeping flow', *Ann. Rev. Fluid Mech.*, **12,** 335–363 (1980).
13. A. T. Chwang and T. Y. Wu, 'Hydromechanics of low-Reynolds-number flow. Part 2. Singularity method for Stokes flows', *J. Fluid Mech.*, **67,** 787–815 (1975).
14. T. Kermanidis, 'A numerical solution for axially symmetrical elasticity problems', *Int. J. Solids Struct.*, **11,** 493–500 (1975).
15. T. A. Cruse, D. W. Snow and R. B. Wilson, 'Numerical solutions in axisymmetric elasticity', *Comp. Struct.*, **7,** 445–451 (1977).
16. S. G. Mikhlin, *Integral Equations*, Pergamon Press, Poland, 1964.
17. D. K. Gartling, R. E. Nickell and R. I. Tanner, 'A finite element convergence study for accelerating flow problems', *Int. J. num. Meth. Engng*, **11,** 1155–1174 (1977).
18. J. Batchelor and F. Horsfall, *Die Swell in Elastic and Viscous Fluids*, Rubber and Plastics Research Association of Great Britain Report 189, 1971.
19. R. E. Nickell, R. I. Tanner and B. Caswell, 'The solution of viscous incompressible jet and free-surface flows using finite-element methods'. *J. Fluid Mech.*, **65,** 189–206 (1974).
20. G. K. Batchelor, *An Introduction to Fluid Mechanics*, Cambridge University Press, Great Britain, 1967.
21. T. Maxworthy, 'Accurate measurements of sphere drag at low Reynolds numbers', *J. Fluid Mech.*, **26,** 369–372 (1965).
22. M. Van Dyke, 'Extension of Goldstein's Series for the Oseen drag of a sphere', *J. Fluid Mech.*, **44,** 365–372 (1970).
23. I. Proudman and J. R. A. Pearson, 'Expansions at small Reynolds numbers for the flow past a sphere and a circular cylinder', *J. Fluid Mech.*, **2,** 237–262 (1957).
24. J. H. Perry, *Chemical Engineers Handbook*, 3 edn, McGraw-Hill, New York, 1950.